



Controls on microbially-induced carbonate precipitation in geologic porous media

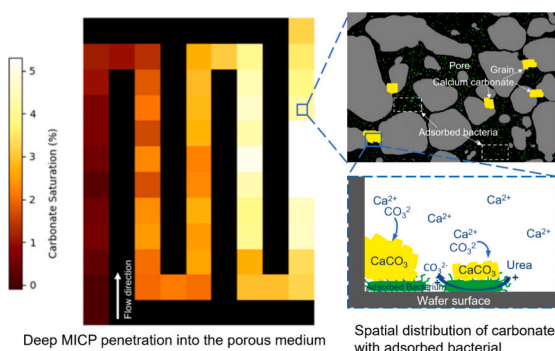
Shunxiang Xia, Wen Song^{*}

Center for Subsurface Energy and the Environment, University of Texas at Austin, 200 East Dean Keeton Street, Austin, TX 78712, United States of America

HIGHLIGHTS

- Novel adsorption mechanism enables uniform delivery of bacteria throughout porous medium.
- Direct spatiotemporal visualization of pore scale carbonate growth.
- Preferential carbonate precipitation at pore throats reduced permeability effectively.
- Extended spatial penetration of microbially-induced carbonate into porous media.

GRAPHICAL ABSTRACT



ARTICLE INFO

Editor: Daniel Alessi

Keywords:

Microbially-induced carbonate precipitation
Microfluidics
Ureolysis
Geologic gas storage

ABSTRACT

Microbially-induced carbonate precipitation (MICP) provides a natural biomineralization approach to secure the geologic storage of gases (e.g., carbon dioxide, hydrogen and methane). Cracks in embrittled wellbore cement, for example, provide a pathway for atmospheric gas leakage, while permeability heterogeneities in the storage reservoir leads to fingering effects that diminish the storage capacity. The design of MICP processes, however, remains a challenge due to limited understanding of the coupled nonlinear reaction kinetics and multiphase transport involved. Specifically, previous attempts at MICP through porous media have been encumbered by carbonate precipitation localized to the first \sim cm of the bulk injection surface. In this study, we investigate the reactive transport controls on MICP necessary to enable deep MICP penetration into the formation. We use a micromodel with pore geometry and geochemistry representative of real geologic media to image direct pore- and pore-ensemble-level mineral, fluid, and microbial distributions. An approach to adsorb microbes uniformly across the micromodel, rather than local accumulation near the inlet, is developed that enables deep MICP penetration into the porous medium. A sensitivity analysis was performed to investigate the impact of injection conditions (e.g., rates, concentrations) required to maximize CaCO_3 precipitation away from the injection site. With multiple cycles of MICP, a \sim 78 % reduction in permeability was achieved with \sim 8 % carbonate pore volume occupation. Overall, this study establishes the possibility of MICP as an effective and controllable method to enhance the security of gas storage in geologic media.

^{*} Corresponding author.

E-mail address: wensong@utexas.edu (W. Song).

<https://doi.org/10.1016/j.scitotenv.2024.177647>

Received 11 July 2024; Received in revised form 7 November 2024; Accepted 17 November 2024

Available online 29 November 2024

0048-9697/© 2024 Published by Elsevier B.V.

Abbreviations

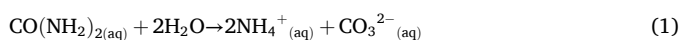
| | |
|---------------------|---------------------------------------------|
| MICP | microbially-induced carbonate precipitation |
| <i>S. pasteurii</i> | <i>Sporosarcina pasteurii</i> |
| OD ₆₆₀ | optical density at 660 nm |
| $v_{\max, b}$ | maximum reaction rate of adsorbed bacteria |
| K_m | Michaelis constant of urea |
| v | reaction rates of ureolysis |
| [c] | concentration of urea |
| PV | pore volume |
| τ | residence time |
| CNN | convolution neural network |
| r | equivalent radius |
| A_c | surface area of crystals |
| V_c | volume of crystals |
| S_{ca} | carbonate saturation |

| | |
|------------|------------------------------------------------------------------------------------------|
| n | kinetics order of bulk carbonate precipitation |
| r_p | bulk precipitate rate of CaCO_3 (M_c , molecular weight of CaCO_3) |
| ρ_c | density of CaCO_3 |
| k_p | bulk kinetic constant of precipitation |
| A_t | sum of all carbonates mineral surface area |
| V_m | molar volume of calcite |
| k_g | growth rate constant of calcite |
| S | supersaturation |
| IP | the ionic product of Ca^{2+} and CO_3^{2-} |
| K_{sp} | solubility product of calcite |
| C_{A0} | initial concentration of urea in cementation solution |
| x_A | conversion rate of urea to CO_3^{2-} |
| v_{\max} | maximum ureolysis reaction rate in micromodel |

1. Introduction

Geologic storage of gases such as carbon dioxide (CO_2), hydrogen (H_2), and methane (CH_4) are critical to mitigating atmospheric greenhouse gas emissions and long duration energy storage (Descoux et al., 2017; Gholami, 2023; Liu et al., 2023a). Field implementation of geologic gas storage, however, is commonly encumbered by two challenges: the development of cracks in embrittled wellbore cement that provide a pathway for pathway for stored gases to the atmosphere, and high permeability pathways that lead to fingering and diminished storage capacity in the reservoir (Kirkland et al., 2021). In both cases, approaches that minimize fluid conductivity in the high permeability flow paths are desired.

Current approaches to cement potential leakage flow paths in storage reservoirs include injection of materials such as cross-linking gels (Kang et al., 2021; Kang et al., 2021; Li et al., 2015) and paraffin waxes (Grisak et al., 1980). These polymeric materials, however, are expensive and chemically unstable under harsh geologic environments (Nasvi et al., 2013). Naturally occurring geologic microbes capable of promoting carbonate precipitation (microbially induced carbonate precipitation, MICP) provide a stable, sustainable, and low-cost alternative to cement leakage pathways to ensure secure geological gas storage (Zhang et al., 2021). Of particular interest are urease-producing bacteria such as *Sporosarcina pasteurii* (*S. pasteurii*) that digest urea ($\text{CO}(\text{NH}_2)_2$) to produce carbonate anions (CO_3^{2-}) (Eq. (1)):



Abundant divalent cations (e.g., Ca^{2+}) dissolved in the formation brine combine with the microbially-secreted CO_3^{2-} to precipitate carbonate minerals (e.g., CaCO_3) as in Eq. (2):



During MICP, carbonate crystallites nucleate preferentially on the microbial cell surfaces of *S. pasteurii* (Hu et al., 2021; Lioliou et al., 2007), where heterogeneous nucleation is encouraged (Oleg S Pokrovsky, 1998). The bacterium *S. pasteurii* was chosen due to its well-documented ability to grow on solid surfaces and its capacity to precipitate calcium carbonate (CaCO_3) minerals under both aerobic and anaerobic conditions (Zhang et al., 2021). Here, MICP is rate-limited by urea degradation (Zhang et al., 2021) and is dependent on microbial density and injection rates rather than the relative concentrations of urea and Ca^{2+} in solution. Co-injections of calcium chloride (CaCl_2) have been identified to maintain an elevated level of bacterial urease activity and CaCO_3 yield (Al Qabany et al., 2012).

Application of MICP toward cementing leakage pathways, however,

remains poorly constrained because of lacking fundamental understanding and control of the coupled mass transfer, cell ureolysis, and precipitation processes. Specifically, the precipitation of carbonate minerals away from the injection site, rather than localized MICP, is needed to seal potential leakage pathways (Minto et al., 2017; Kirkland et al., 2021; Phillips et al., 2018). While past studies in porous media show that MICP can reduce matrix permeability by up to 8 orders of magnitude (Yu et al., 2021), these minerals precipitate typically within \sim cm of the bulk injection surface and lack penetration into the storage formation (Ferris et al., 2003; Liu et al., 2023a; Mortensen et al., 2011; Pokrovsky, 1998; Zhang et al., 2021). Core experiments suggest microbial aggregation in pore throats that alter flow and bacteria distribution patterns and result in localized CaCO_3 growth (Cui et al., 2017). Control over geologic MICP rates and spatial distributions are further complicated by elevated reservoir temperatures, complex water composition, bacteria-mineral interactions (Gao et al., 2024), and local flow behavior (Zhang et al., 2021). The influence of these complex systems on MICP requires spatiotemporal resolution of the fundamental pore-scale processes that have so far been inaccessible to core-level experiments. Another concern with the application of MICP is the potential environmental and groundwater impacts resulting from the byproducts of urea hydrolysis. When urea breaks down during MICP, ammonium (NH_4^+) is produced and may lead to ammonium contamination, nitrate formation, and increased salinity. To minimize these potential environmental risks, MICP must be conducted efficiently and with a high degree of control (Konstantinou and Wang, 2023).

Recent advances in microfluidic platforms with pore geometry and surface chemistry representative of geologic media, coupled with optical microscopy and advanced analytical approaches such as Raman spectroscopy, provide an approach to study the fundamental pore-level interactions between microbes and cementation fluids in confined geologic environments (Liu et al., 2023b; Song et al., 2014; Xia et al., 2023). While polymeric microfluidics (e.g., polydimethylsiloxane, PDMS) have been used to study the relationship between solution chemistry and MICP kinetics (Xiao et al., 2021), they lack the representative mineral surface characteristics to elucidate microbe-mineral interactions.

In this study, we investigate the mechanisms controlling microbial and MICP distributions in geologic materials using a tortuous etched-silicon micromodel with representative pore geometry of a sandstone (Fig. 1). Solution chemistry and flow rates are tuned to distribute the microbes and to precipitate carbonates throughout the micromodel. We investigate the spatial controls on microbially-induced carbonate precipitation that reduce fluid conductivity in high-permeability flow paths. We leverage a new surface adsorption mechanism to distribute the bacteria uniformly across the micromodel rather than localized

accumulation near the inlet. This, combined with controls on the rates of carbonate precipitation, microbial activity, and reagent transport, enables deep MICP penetration to cement preferential flow paths that may otherwise facilitate stored gas leakage.

2. Material and methods

2.1. Micromodel fabrication

Pore-scale visualization of MICP was achieved using an etched-silicon micromodel with pore geometry representative of sandstone (porosity $\sim 54\%$, permeability 800 mD) following photolithography and ion etching techniques developed in previous work (c.f., Song and Kovscek, 2015, 2016, 2019; Song et al., 2018). In short, a silicon wafer (University Wafer Inc.) was etched to a depth of 10 μm using the Bosch process (Plasma Lab 80+, Oxford Instruments) with average pore body and throat sizes of 58 and 13 μm , respectively (Fig. 1c). A total porous medium length of 115 mm was achieved using a tortuous configuration (Fig. 1b). The etched wafer, with drilled inlet and outlet flow ports, was bonded anodically to Schott Borofloat 33 glass (thickness ~ 1 mm, University Wafer Inc.) to enable flow confinement and direct optical visualization.

2.2. Bacteria culturing and characterization of the ureolysis reaction

In this study, *Sporosarcina pasteurii* (*S. pasteurii*, ATCC 11859) was chosen for its ability to secrete CO_3^{2-} and to precipitate CaCO_3 . A growth medium was prepared by mixing 20 g of yeast extract (CAS-NO: 8013012, MilliporeSigma) and 10 g of ammonium sulfate (CAS-NO: 7783202, Sigma-Aldrich) in 1 L of deionized (DI) water. The mixture was sterilized at 121 $^\circ\text{C}$ for 15 mins in an autoclave. *S. pasteurii* was then inoculated in the growth medium and incubated at room temperature for three days to encourage growth. Subsequently, the bacterial broth was centrifuged at 3000 rpm for 5 mins, and the cells were collected and re-suspended in a 20,000 ppm sodium chloride brine (NaCl, CAS 7647-14-5, Sigma-Aldrich) to achieve ~ 0.8 OD₆₆₀ (the optical density at 660 nm measured using UV-vis spectroscopy).

To determine microbial activity within porous geologic media, we characterized the kinetics of ureolysis catalyzed by *S. pasteurii* that are adsorbed on silica surfaces. We begin by pipetting 50 μL of cell suspension and 50 μL of a 200 mM CaCl_2 solution onto the surface of an oxidized silicon wafer. The mixture was kept acquiescent (i.e., static) for 2 h to enable microbial adsorption onto the silicate surface. The wafer surface was then washed three times with 100 mM CaCl_2 to remove any mobile (i.e., not adsorbed) bacteria. To initiate microbial ureolysis, 100 μL of urea solution with concentrations of $[S] \sim 0.25, 0.5, 1, 2,$ and 4 M

were applied to the bacteria-adsorbed surface (~ 2 cm^2 reaction area) (Fig. S1a). Ureolysis reaction rates, v , were determined by measuring the concentration of NH_4^+ in the reaction solution after 2 h using the Berthelot method. To determine the maximum ureolysis rate of the adsorbed bacteria, $v_{\text{max},b}$, and the Michaelis constant of urea, K_m , the reaction rate data were plotted (Lineweaver–Burk plot, $1/v$ vs. $1/[S]$) to generate a straight line where the intercept was $1/v_{\text{max},b}$ and the slope was $K_m/v_{\text{max},b}$ (Fig. S1b). The cell density was calculated by counting the number of adsorbed cells in the field of view under darkfield imaging.

2.3. MICP in the micromodel

The micromodel was injected with brine (20,000 ppm NaCl in DI water) using syringe pumps (Harvard Apparatus) until all air was removed. To initiate MICP, two pore volumes (PV) of bacteria suspension and fixation solution (200 mM CaCl_2) were co-injected at 10 m/day, in keeping with near-well fluid velocities. The micromodel was then kept static for 2 h to encourage microbial adsorption. Following this, 2 PV of fixation solution was injected at 2 m/day to wash out any mobile bacteria (i.e., those not adsorbed to a pore surface). Precipitation of CaCO_3 was initiated by injecting a cementation solution containing Ca^{2+} and urea into the micromodel. The influence of urea concentration and injection velocity on the precipitation rate and spatial distribution of CaCO_3 was assessed by continuously injecting 1 M CaCl_2 solutions for a range of urea concentrations (i.e., 2, 1, and 0.5 M urea corresponding to 3.7, 1.85, and 0.92 $[c]/K_m$) at a range of superficial velocities (0.5, 1, 2, and 4 m/day, corresponding to 3.82, 1.62, 0.81, and 0.41 times the residence time $\tau = V_{\text{pore}}/\text{injection rate}$). For multiple cycles of MICP, bacteria suspension and fixation solution injections commenced following the completion of the previous injection stage. The permeability reduction after each cycle of MICP was calculated based on the pressure drop monitored by a pressure sensor (uPS0800-C360-10, LabSmith) during the injection of a single-phase 1 M CaCl_2 aqueous solution at a superficial velocity of 1 m/day. The mineral compositions of precipitated carbonates after 1, 4, and 8 h of cementation were visualized and analyzed using an optical light microscope (Nikon Eclipse Lvdia-N) and camera (Nikon Ds-fi3) system paired with a micro-Raman spectroscope (Horiba iHR320, Fig. 1a). Large whole-micromodel images were captured every 4 h, over a total of 24 h, to visualize the pore- and pore-ensemble growths of CaCO_3 within the porous medium. Bacteria transport and CaCO_3 precipitation were monitored using darkfield and polarized light microscopy, respectively. Microbially-induced carbonate nucleation at early stages of MICP was characterized by scanning electron microscopy (SEM, FEI Quanta 650 ESEM) of an opened micromodel. All experiments were performed at ambient conditions (~ 1 atm, 25 $^\circ\text{C}$). We note here that while these pressures and temperatures are

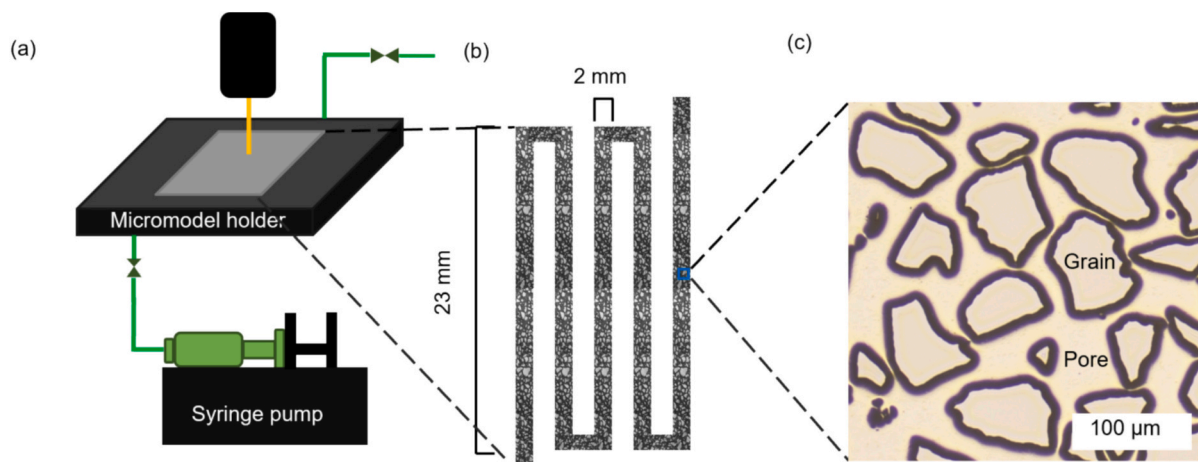


Fig. 1. (a) Schematic of the microvisualization platform. (b) Tortuous micromodel with 115 mm of total flow length. (c) Pore structure of etched silicon wafer.

lower than those of deep storage formations, the effect of pressure on MICP is minimal and the effect of elevated temperatures acts primarily on enhancing the rate of ureolysis (Zhang et al., 2021).

2.4. Image processing

Quantification of MICP kinetics and distribution (micrographs $\sim 20,480 \mu\text{m} \times 28,160 \mu\text{m}$, 1 pixel equals $1 \mu\text{m}$) was achieved by image segmentation using an in-house convolution neural network (CNN)-based image processing algorithm (Davletshin et al., 2021). Carbonate is bright under polarized light and is distinguishable easily from the dark silica grains. The original images were first cropped and binarized, and the outline of carbonates was detected to obtain the equivalent radius, r , of CaCO_3 crystals (Fig. S2). Assuming a semispherical shape of the carbonate crystals (c.f., Kim et al., 2020, confirmed in this study with SEM micrographs, Fig. 3a), the surface area, A_c , and volume, V_c , of the crystals were calculated based on r and etching depth ($10 \mu\text{m}$) using the following equations:

$$\begin{cases} A_c = 2\pi r^2 \text{ for } r \leq 10 \mu\text{m} \\ A_c = 20\pi r \text{ for } r > 10 \mu\text{m} \end{cases} \quad (3)$$

$$\begin{cases} V_c = \frac{2}{3}\pi r^3 \text{ for } r \leq 10 \mu\text{m} \\ V_c = \pi(10r^2 - 1000/3) \text{ for } r > 10 \mu\text{m} \end{cases} \quad (4)$$

Average carbonate precipitate saturation, S_{ca} , in the micromodel was calculated as the ratio of the total volume occupied by CaCO_3 , $V_c(t)$, to the initial pore volume $V_p(t_0)$.

2.5. Assessing kinetics of carbonate precipitation

To investigate the spatial heterogeneity of in situ carbonate growth, the micromodel is divided into five equal segments and quantified individually. The kinetics order of bulk carbonate precipitation, n , is calculated using:

$$r_p = k_p(S - 1)^n \quad (5)$$

where r_p is the bulk precipitation rate of CaCO_3 defined as the change in mole of CaCO_3 per pore volume per unit time, k_p is the bulk kinetic constant of precipitation, and S is the supersaturation of CaCO_3 . Specifically, the bulk kinetic constant of precipitation (k_p) is calculated as:

$$k_p = k_g A_t / V_m \quad (6)$$

where A_t is the sum of all carbonate mineral surface areas and V_m is the molar volume of calcite ($0.0369 \text{ m}^3 \text{ kmol}^{-1}$). Over 24 h, the growth rate constant, k_g , is approximated by that of calcite ($10^{-11} \text{ m s}^{-1}$) (Kralj et al., 1997). Supersaturation, S , is calculated using following:

$$S = (IP/K_{sp})^{1/2} \quad (7)$$

where IP is the ionic product of Ca^{2+} and CO_3^{2-} , and K_{sp} is the solubility product of calcite ($K_{sp} \sim 10^{-8.48}$) (Gal et al., 1996).

To calculate the concentration of CO_3^{2-} ions, $C_{A0}x_A$, the bacteria-adsorbed micromodel is modelled as plug flow reactor. Here, the diffusion of urea in water is $1.38 \times 10^{-5} \text{ cm}^2/\text{s}$, and for interstitial velocities of 3.7 m/day, does not introduce significant dispersion effects (Péclet number ~ 1000) (Nanne et al., 2010):

$$C_{A0}x_A - K_m \ln(1 - x_A) = v_{max}\tau \quad (8)$$

where C_{A0} is the initial concentration of urea in the cementation solution, x_A is the conversion rate of urea to CO_3^{2-} , K_m is the Michaelis constant of the ureolysis reaction catalyzed by *S. pasteurii* (i.e., 0.54 M), v_{max} is the maximum ureolysis reaction rate in micromodel ($v_{max} = v_{max,b}$ / etching depth $\sim 0.11 \text{ kmol}/\text{m}^3/\text{h}$), and τ is the residence time ($\tau =$

$V_{\text{pore volume}} / \text{injection rate}$).

3. Results and discussion

3.1. Retention of bacteria in porous media

Distributed growth of microbially precipitated carbonates is crucial to ensuring effective sealing of potential leakage pathways in geologic gas storage reservoirs. Control on the spatial penetration of MICP in the geologic formation is determined by the ability to disperse and retain microbes throughout the porous medium. Key questions remain, however, on the underlying microbe-mineral-fluid interactions that control bacteria retention. To distribute the microbes uniformly into the formation, we immobilized the bacteria via a new surface adsorption mechanism (Fig. 2b) rather than current pore-clogging approaches (Fig. 2c). A key challenge with the surface attachment of *S. pasteurii*, however, is its negative surface charge at low cationic concentrations (Ma et al., 2020). Specifically, the electric repulsive forces between the surface of sand grains (SiO^-) and the bacteria discourage microbial adsorption (Fig. 2a).

Here, we co-inject a 200 mM calcium chloride (CaCl_2) solution to neutralize the surface charge of the bacteria and to enable microbial adsorption onto pore surfaces (Fig. 2a) (Ma et al., 2020). After 2 h of equilibration, a single layer of bacteria was attached stably on the silica surface across the entire length of the micromodel (Fig. 2b). Surface adherence of the adsorbed bacteria was confirmed by additional injection of 2 PV of the fixation solution into the micromodel at 2 m/day. Here, the surface density of adsorbed bacteria increased with the concentration of Ca^{2+} in the fixation solution (Fig. 2d). For example, co-injecting a fixation solution with 1 mM Ca^{2+} adsorbed ~ 244 bacteria/ mm^2 , while the surface density of adsorbed bacteria increased to 3118 bacteria/ mm^2 with a 100 mM Ca^{2+} solution. Further increases in Ca^{2+} concentration along with slow fluid velocities (e.g., 200 mM CaCl_2 at 1 m/day), however, led to microbial aggregation and clogging in narrow flow paths near the injection port (Fig. 2c). Clogging and subsequent accumulation of microbes, counterproductively, leads to increased rates of local MICP that limits the delivery of bacteria and reactants into the reservoir, and, ultimately reduces the MICP penetration distance. The near-injection cementation leads to fails to reduce the permeability of the entire leakage pathway, leading to poor control over the fate of migrating fluids (Phillips et al., 2013).

3.2. Nucleation and growth of carbonates at the pore scale

To understand the pore-level reactive transport controls that enable penetration of MICP processes into the flow path, bacteria-mediated nucleation and growth characteristics of CaCO_3 were visualized in the micromodel. Immediately following the injection of the CaCl_2 cementation fluid, *S. pasteurii* ureolysis resulted in the nucleation of carbonate grains on the surface of bacteria (Fig. 3a). We note that MICP initiates on particle surfaces where carbonate grains are immobile. The newly formed crystals were spherical in shape, with Raman shifts at 1071 cm^{-1} that correspond to vaterite (Fig. 3a, d).

With CaCO_3 growth, Raman spectroscopy of the crystals also showed an increasing peak at 1085 cm^{-1} that corresponds to calcite. Here, we find that the crystal growth process was governed by thermodynamics, where calcite with lower Gibbs free energy is the more stable form of CaCO_3 (Boulos et al., 2014). Later stages of MICP, however, show that the accumulation of carbonates surrounding the bacteria forms a CaCO_3 shell (Fig. 3b) that isolates the cell from the bulk fluid environment. This physical isolation limits nutrient supply and leads to eventual cell death and slowing overall rates of MICP. After 24 h of cementation, most carbonate crystals are rhombohedral, characteristic of calcite, with equivalent diameters exceeding $30 \mu\text{m}$ (Fig. 3b).

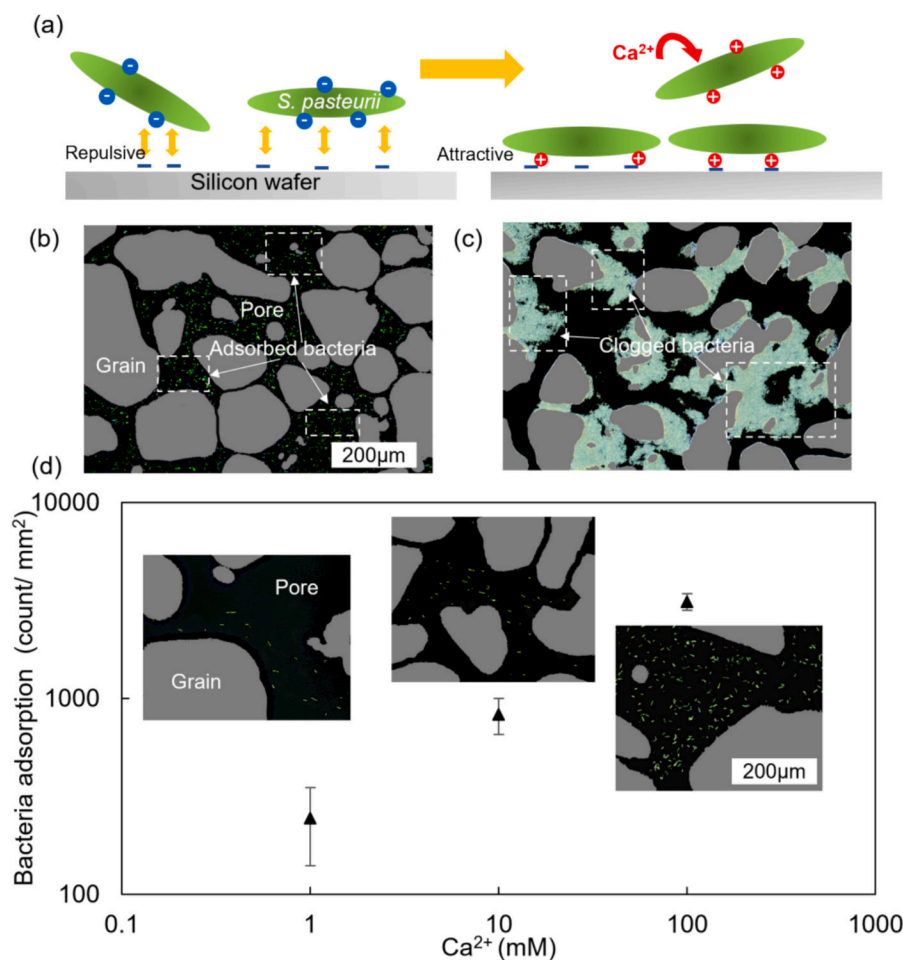


Fig. 2. (a) Schematic of bacteria adsorption on negatively charged silica surfaces with (right) and without (left) Ca^{2+} ions. (b) Bacteria adsorbed along pore surfaces developed here. (c) Bacteria clogged in pore throats as in previous studies. (d) The effect of Ca^{2+} concentration on bacteria adsorption density. The grain and bacteria are denoted by gray and green, respectively.

3.3. Kinetics of carbonate precipitation

Homogeneous microbe distribution across the length of the micro-model provides an opportunity to enable deep MICP penetration into the formation. In all 5 segments along the micromodel, the bulk CaCO_3 precipitation rate, r_p , remained constant during the first 12 h before slowing and eventually stopping after 24 h of cementation (Fig. 4). Here, slowing precipitation kinetics are attributed to cell starvation and urease loss following the encapsulation of the microbe by growing carbonate crystals (Fig. 3b). Notably, we observed greater r_p downstream of the injector ($0.085 \text{ kmol m}^{-3} \text{ h}^{-1}$ in segment 5 and $0.032 \text{ kmol m}^{-3} \text{ h}^{-1}$ in segment 1) (Table 1) where supersaturations are elevated ($S \sim 2589$ in segment 5 and 1037 in segment 1). In the first segment, the concentration of carbonate ions, generated from ureolysis, was too low to sustain MICP. As carbonate ions accumulate downstream, the availability of CO_3^{2-} enables a high r_p . Post MICP, CaCO_3 occupied $\sim 4.2\%$ of the pore volume in downstream segments, significantly higher than those near the inlet (i.e., $\sim 1.3\%$). According to Eq. 6, the 4th and 5th segments exhibited higher k_p where more crystal surfaces (A_t) were available for CaCO_3 growth ($k_p \sim 6.26 \cdot 10^{-6} \text{ kmol/m}^3 \text{ h}$ with $A_t \sim 2253.61 \text{ m}^{-1}$ in segment 5 vs. $k_p \sim 2.24 \cdot 10^{-6} \text{ kmol/m}^3 \text{ h}$ with $A_t \sim 805.72 \text{ m}^{-1}$ in segment 1) (Table 1). Typically, first-order precipitation reactions (e.g., $n = 1$) are controlled by diffusion (Pokrovsky et al., 2005) while second-order reactions (e.g., $n = 2$) are used to model CaCO_3 precipitation under supersaturated conditions (Dawe and Zhang, 1997). In this study, we calculate n to be ~ 1.2 , which suggests that the

diffusion of carbonate ions, limited by ureolysis, controls the rate of CaCO_3 precipitation during MICP. While MICP has been studied extensively, controlling the spatial kinetics of carbonate precipitation remains a significant challenge (Zhang et al., 2021). Our study provides critical insights into the reactive transport controls necessary for achieving a uniform MICP, which has not been characterized previously.

3.4. Spatial distribution of carbonate minerals in high permeability flow paths

Slow precipitation rates near the inlet enabled MICP away from the injection site, critical to cementing leakage pathways in embrittled wellbore materials. Unlike in shallow soil systems where MICP occurs under static (no flow) conditions, here we inject cementation solutions continuously for 24 h to suppress MICP near the injection site and to encourage distal carbonate growth. Specifically, the local S_{ca} (i.e., pore volume occupancy of the CaCO_3) in the micromodel ranged from ~ 0.1 to 5.2% as a function of distance from the injection site, with an average of $S_{\text{ca}} \sim 2.7\%$ (Fig. 5). MICP suppression near the inlet ($S_{\text{ca}} \sim 0.1\%$) and enhancement downstream ($S_{\text{ca}} \sim 5.2\%$) is a result of the competition between ureolysis, local CO_3^{2-} availability, and carbonate precipitation. Here, ureolysis is the rate-limiting step, and sufficient time is required for *S. pasteurii* to digest urea and produce sufficient CO_3^{2-} for carbonate precipitation. As a result, continuous injection of CaCl_2 precipitated only a trace amount of CaCO_3 in the first segment of the micromodel ($S_{\text{ca}} \sim 1.3\%$). In contrast, high S_{ca} were measured downstream (e.g., $S_{\text{ca}} \sim 4.2$

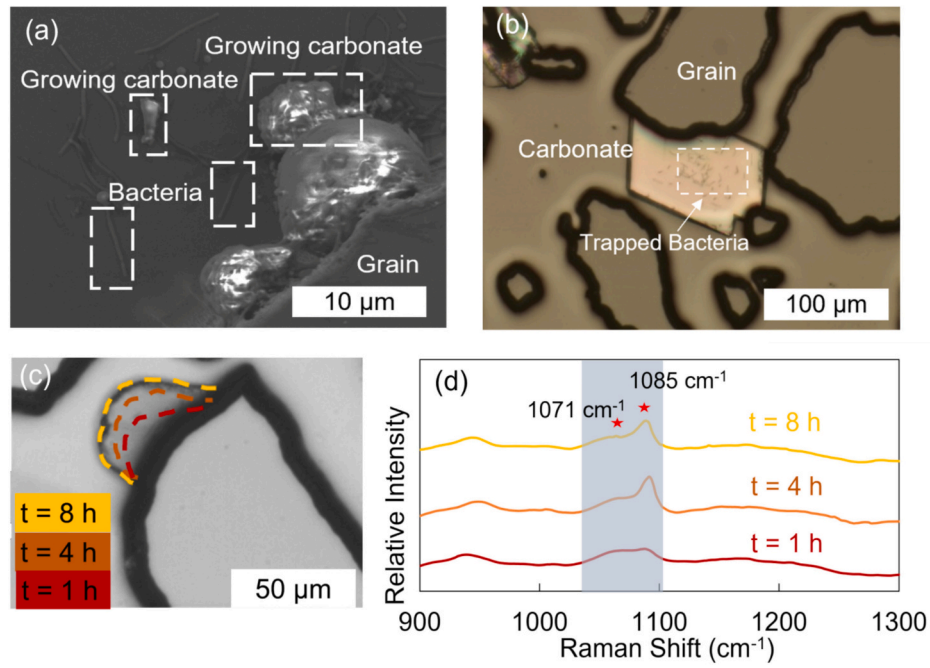


Fig. 3. (a) SEM of CaCO_3 nucleation and growth after 1 h of cementation. (b) Focusing on the bacteria in the z-plane showed that *S. pasteurii* are trapped within the CaCO_3 crystals after 24 h of cementation. (c) Growth of a single CaCO_3 crystal in time. (d) Raman spectra of the CaCO_3 phase imaged in (c) after 1, 4, 8 h of cementation show a shift from vaterite (1071 cm^{-1} and 1085 cm^{-1}) at early times to calcite (1085 cm^{-1}) after 4 and 8 h of growth.

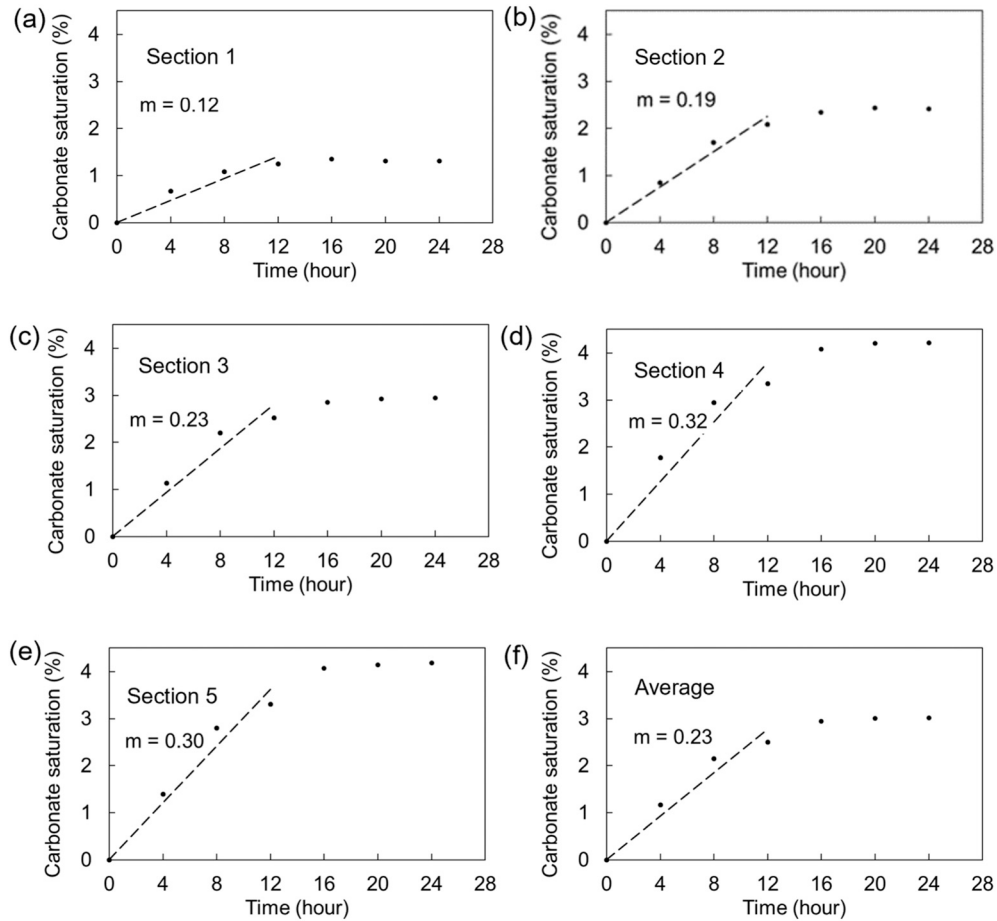


Fig. 4. Carbonate saturation as a function of cementation times for the five micromodel segments (a-e) and for the entire micromodel (f). The rate of precipitation was calculated by measuring the slope, m , for the first 12 h of cementation.

Table 1Precipitation parameters of CaCO_3 of the five segments of the micromodel during 12 h of MICP.

| | Segment 1 | Segment 2 | Segment 3 | Segment 4 | Segment 5 |
|-------------------------------------------------------|-----------|-----------|-----------|-----------|-----------|
| r_p ($\text{kmol m}^{-3} \text{h}^{-1}$) | 0.032 | 0.054 | 0.065 | 0.086 | 0.085 |
| A_t (m^{-1}) | 805.72 | 1296.65 | 1756.17 | 2525.56 | 2253.61 |
| S | 1036.06 | 2180.90 | 2582.35 | 2656.32 | 2589.02 |
| k_p ($10^{-6} \text{ kmol m}^{-3} \text{h}^{-1}$) | 2.24 | 3.6 | 4.88 | 7.02 | 6.26 |
| n | 1.38 | 1.25 | 1.20 | 1.19 | 1.21 |

% for both segments 4 and 5), where MICP rates plateaued as a result of CO_3^{2-} availability and sufficient residence time for carbonate precipitation. We note, however, that heterogeneities exist within each segment as a result of the meandering macroscopic geometry of the porous medium. Previous studies have highlighted challenges in achieving deep MICP penetration due to localized carbonate precipitation near injection

sites (Ferris et al., 2003; Mortensen et al., 2011). Our approach overcomes this limitation by employing a novel bacterial adsorption mechanism where cementation fluids are injected continuously. Specifically, carbonate precipitates nucleate and grow uniformly in the porous medium (i.e., away from the injection site).

The influence of urea concentration (indicated by $[c]/K_m$) and

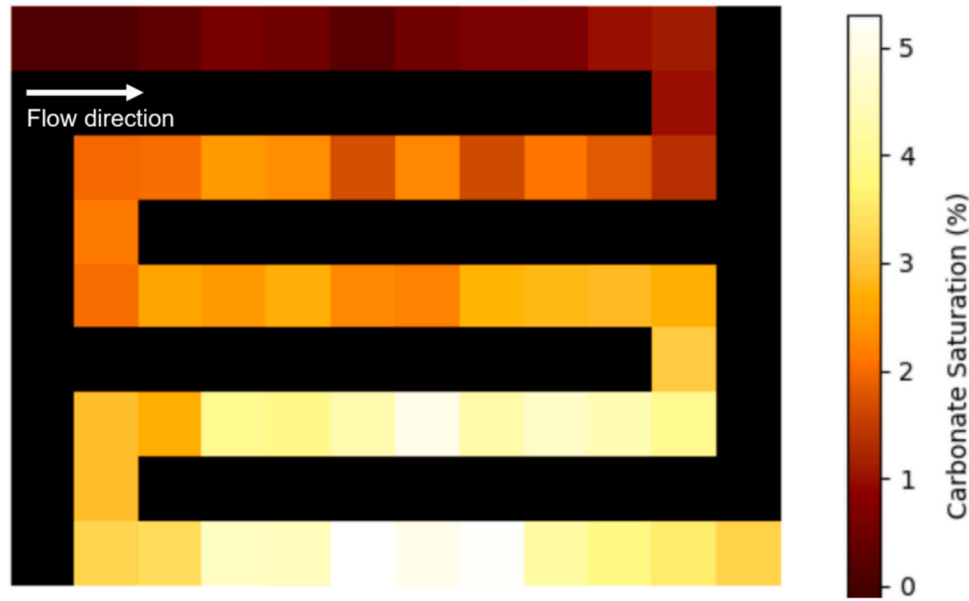


Fig. 5. A heatmap of carbonate saturation ($S_{ca} = V_{\text{CaCO}_3}/V_{\text{pore}}$) across the entire micromodel after 24 h of MICP showing delayed precipitation near the inlet and spatial penetration ($> \text{cm}$) of CaCO_3 precipitates in the porous medium. Here, cementation fluid containing 1 M CaCl_2 and 2 M urea is injected at 1 m/day. The flow direction is denoted by the white arrow. Experiments were conducted in triplicate.

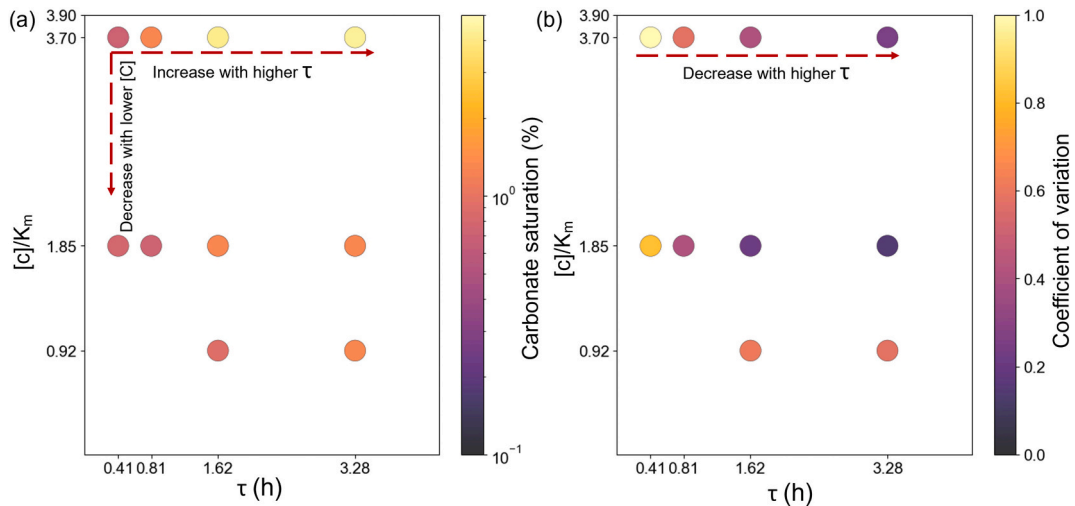


Fig. 6. Carbonate saturation (S_{ca}) of micromodel sections containing the greatest level of precipitation (a) and coefficient of variation of carbonate saturation (b) of MICP by injecting 1 M CaCl_2 solutions with concentrations of 2, 1, and 0.5 M urea (i.e., corresponding to 3.7, 1.85 and 0.92 $[c]/K_m$) at superficial velocities of 0.5, 1, and 2 and 4 m/day (i.e., corresponding to 3.82, 1.62, 0.81 and 0.41 τ (h)). Data for the full set of experiments is taken from single experimental runs, however multiplicates were performed that show similar trends.

residence time (τ) on MICP was assessed to enhance the spatial extent of carbonate precipitation (Fig. 6a). In all experiments, downstream segments (i.e., segments 4 and 5) showed the highest S_{ca} , indicating successful penetration of carbonate minerals into the flow path. For a single MICP injection cycle, the greatest level of MICP ($S_{ca} \sim 4.3\%$ in Section 4) was achieved by injecting a cementation fluid containing 3.7 [c]/K_m of urea at velocities of $\tau \sim 3.28\text{ h}$. Decreasing urea concentrations resulted in reduced MICP volumes ($S_{ca} \sim 1.3\%$ at 1.85 [c]/K_m and 1.3% at 0.92 [c]/K_m , in Section 4). Similarly, shorter τ (i.e., faster injection velocities) also diminished the extent of MICP ($S_{ca} \sim 4.1\%$ in Section 4, 1.3% in section 5, and 0.8% in section 5 for τ of 1.62, 0.81 and 0.41 h).

Poor control over the penetration of carbonate precipitation in porous media has been a persistent challenge in MICP-based cementation processes (DeJong et al., 2010; Fu et al., 2023). Through direct visualization in this study, we show that MICP heterogeneity stems from the delayed precipitation of CaCO_3 in the initial segments of the micromodel. Higher S_{ca} heterogeneity indicates better penetration, as a greater percentage of CaCO_3 was precipitated downstream.

The coefficient of variation (e.g., standard deviation/mean) of CaCO_3 precipitation within five segments of the micromodel were calculated and used to assess heterogeneity (Fig. 6b). Overall, decreasing the residence time, τ , resulted in a more heterogeneous distribution of CaCO_3 . For instance, at $[\text{c}]/\text{K}_m \sim 3.7$, the coefficients of variation for carbonate growth across the micromodel were 0.25, 0.41, 0.58, and 1.02 for $\tau \sim 3.28, 1.62, 0.81$, and 0.41 h , respectively. Under realistic conditions, the design of MICP should also consider the effect of complex flow regimes (e.g., radial flow), spatial complexity, and operational limitations (Yu et al., 2021). Nevertheless, our results provide insights into understanding how parameters of reactive transport influence the spatial control of MICP, serving as a bridge between theoretical frameworks and field application.

3.5. Permeability reduction with multiple cycles of MICP

To assess the cementation performance of MICP, multiple cycles of

injection were performed to calculate the corresponding permeability reduction. We find that S_{ca} increases in each cycle, and results in an overall decrease in permeability (Fig. 7a,b). After the first cycle, CaCO_3 occupied $\sim 3.1\%$ of the pore volume and decreased the total permeability by $\sim 10\%$. Two subsequent cycles of MICP further increased the total carbonate saturation to $\sim 4.7\%$, which led to a 66% decrease from the initial permeability. Additional cycles led primarily to the growth of existing carbonate mineral grains rather than the nucleation of new crystals (Fig. 7c). We note here that in cases where the initial pore surfaces are coated with carbonate minerals, subsequent MICP cycling is not limited by the number of available nucleation sites, resulting in homogeneous growth and the formation of carbonate bridge structures (Song et al., 2022). In contrast to the homogenous microbial adsorption observed in the first cycle, preferential adsorption of bacteria on CaCO_3 surfaces was observed in later cycles. The uneven adsorption of bacteria, along with the high surface energy of CaCO_3 , resulted in preferential MICP on existing CaCO_3 grains rather than negatively charged silicate surfaces. The different adsorption behavior of *S. pasteurii*, as shown here, suggests that microbial delivery and retention, and, hence MICP performance, is dependent upon the mineralogy of the formation. For clean sandstones as in the experiments here, co-injecting Ca^{2+} ions counteract the negative surface charge of the silica that makes spontaneous microbial adsorption unfavorable. Carbonate grains, on the other hand, provide a positively charged surface that enables *S. pasteurii* adsorption. After 6 cycles of MICP, the formation permeability was reduced by $\sim 78\%$, albeit only a total carbonate saturation of $\sim 8\%$. Permeability was reduced to $k \sim 0$ after 7 cycles. Micromodel imaging shows that CaCO_3 precipitated selectively in pore throats rather than pore bodies to alter the flow path and reduce the overall permeability (Fig. 7c).

Scaling up from micromodels to actual reservoir implementation will require careful consideration of factors such as reservoir heterogeneity, microbial survival under subsurface conditions, and fluid dynamics. Data from pilot studies will provide insights on the feasibility of our approach in securing geologic gas storage and should be the focus of future research.

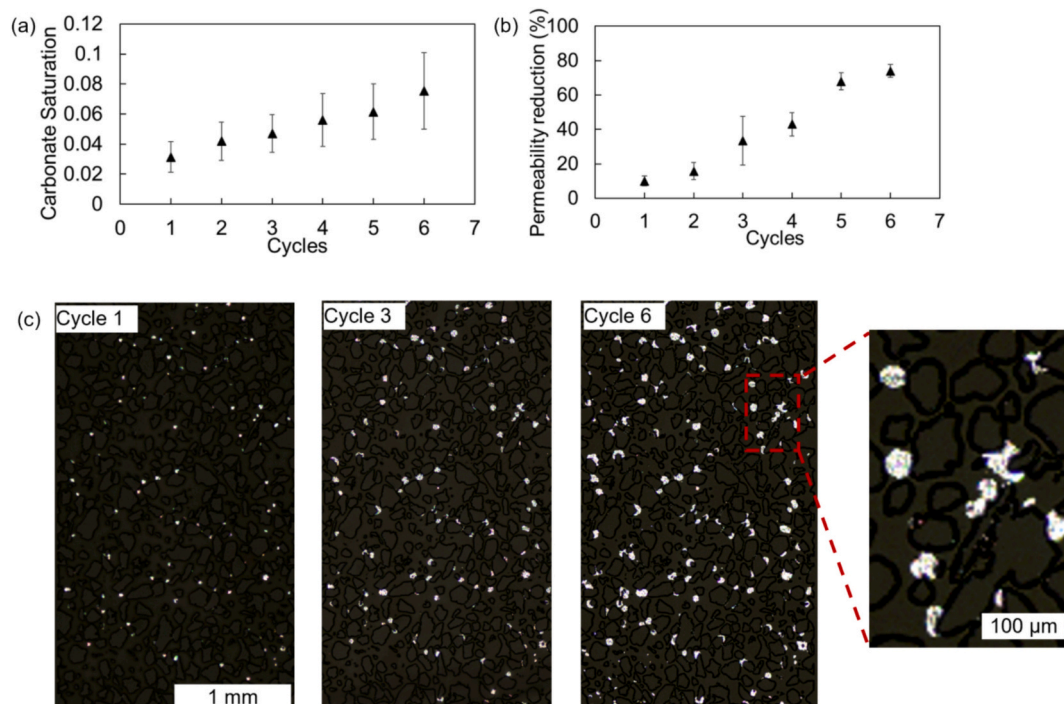


Fig. 7. Carbonate saturation S_{ca} (a) and permeability reduction (b) after multiple cycles of MICP. (c) The distribution of carbonate within micromodel after 1, 3 and 6 cycles of MICP. The enlarged view shows that carbonate precipitate primarily in pore throats. Carbonate precipitates are denoted in white. Experiments were conducted in triplicate.

4. Conclusion

In this study, we developed a microfluidic device with pore geometry and geochemistry representative of real geologic media to investigate the spatial distribution and rate of MICP. We demonstrated the feasibility of retaining bacteria within pore media through adsorption, aiming for the uniform delivery of bacteria and reactants over distance. CaCO_3 precipitation was delayed near the inlet, unlike previous studies where MICP was limited to the first \sim cm of injection. We performed a sensitivity analysis on CaCO_3 precipitation as function of injection rate and concentration of cementation fluid and revealed that MICP was limited by the rate of microbial urea decomposition, therefore affecting its spatial distribution into the reservoir. Importantly, the permeability of the porous media was reduced by \sim 78 % with only \sim 8 % carbonate saturation after six cycles of MICP. The study proves the potential of MICP as an efficient and controllable cementation process, bringing insight into the understanding of key mechanisms of reaction kinetics and multiphase reactive transport during MICP before scaling up.

CRediT authorship contribution statement

Shunxiang Xia: Writing – review & editing, Writing – original draft, Visualization, Methodology, Investigation, Formal analysis, Data curation, Conceptualization. **Wen Song:** Writing – review & editing, Supervision, Resources, Project administration, Funding acquisition, Formal analysis, Conceptualization.

Declaration of competing interest

The authors declare that they have no known competing financial interests or personal relationships that could have appeared to influence the work reported in this paper.

Acknowledgements

The authors gratefully acknowledge support in part from the United States Department of Energy (FE0031791, FE0032349) and the University of Texas at Austin Energy Institute.

Appendix A. Supplementary data

Supplementary data to this article can be found online at <https://doi.org/10.1016/j.scitotenv.2024.177647>.

Data availability

Data will be made available on request.

References

- Al Qabany, A., Soga, K., Santamarina, C., 2012. Factors affecting efficiency of microbially induced calcite precipitation. *J. Geotech. Geoenviron. Eng.* 138, 992–1001. [https://doi.org/10.1061/\(asce\)gt.1943-5606.0000666](https://doi.org/10.1061/(asce)gt.1943-5606.0000666).
- Boulos, R.A., Zhang, F., Tjandra, E.S., Martin, A.D., Spagnoli, D., Raston, C.L., 2014. Spinning up the polymorphs of calcium carbonate. *Sci. Rep.* 4. <https://doi.org/10.1038/srep03616>.
- Cui, M.J., Zheng, J.J., Zhang, R.J., Lai, H.J., Zhang, J., 2017. Influence of cementation level on the strength behaviour of bio-cemented sand. *Acta Geotech.* 12, 971–986. <https://doi.org/10.1007/s11440-017-0574-9>.
- Davletshin, A., Ko, L.T., Milliken, K., Periwai, P., Wang, C.C., Song, W., 2021. Detection of framboidal pyrite size distributions using convolutional neural networks. *Mar. Pet. Geol.* 132. <https://doi.org/10.1016/j.marpetgeo.2021.105159>.
- Dawe, R.A., Zhang, Y., 1997. Kinetics of calcium carbonate scaling using observations from glass micromodels. *J. Pet. Sci. Eng.* 18 (3–4), 179–187.
- DeJong, J.T., Mortensen, B.M., Martinez, B.C., Nelson, D.C., 2010. Bio-mediated soil improvement. *Ecol. Eng.* 36, 197–210. <https://doi.org/10.1016/j.ecoleng.2008.12.029>.
- Descloux, S., Chanudet, V., Serça, D., Guérin, F., 2017. Methane and nitrous oxide annual emissions from an old eutrophic temperate reservoir. *Sci. Total Environ.* 598, 959–972. <https://doi.org/10.1016/j.scitotenv.2017.04.066>.
- Ferris, F.G., Phoenix, V., Fujita, Y., Smith, R.W., 2003. Kinetics of Calcite Precipitation Induced by Ureolytic bacteria at 10 to 20°C in Artificial Groundwater. [https://doi.org/10.1016/S0016-7037\(00\)00503-9](https://doi.org/10.1016/S0016-7037(00)00503-9).
- Fu, T., Saracho, A.C., Haigh, S.K., 2023. Microbially induced carbonate precipitation (MICP) for soil strengthening: a comprehensive review. *Biogeotechnics* 1, 100002. <https://doi.org/10.1016/j.bgtech.2023.100002>.
- Gal, J.-Y., Bollingerb, J.-C., Tolosa, H., Gache, N., 1996. Calcium carbonate solubility: a reappraisal of scale formation and inhibition. *Talanta* 43 (9), 1497–1509.
- Gao, X., Han, Z., Zhao, Y., Zhang, J., Zhai, D., Li, J., Qin, Y., Liu, F., Wang, Q., Steiner, M., Han, C., 2024. Microbial-mineral interaction experiments and density functional theory calculations revealing accelerating effects for the dolomitization of calcite surfaces by organic components. *Sci. Total Environ.* 915. <https://doi.org/10.1016/j.scitotenv.2024.169971>.
- Gholami, R., 2023. Hydrogen storage in geological porous media: solubility, mineral trapping, H₂S generation and salt precipitation. *J. Energy Storage* 59. <https://doi.org/10.1016/j.est.2022.106576>.
- Grisak, G.E., Pickens, J.F., Cherry, J.A., 1980. Solute transport through fractured media: 2. Column study of fractured till. *Water Resour. Res.* 16, 731–739. <https://doi.org/10.1029/WR016i004p00731>.
- Hu, L., Wang, H., Xu, P., Zhang, Y., 2021. Biomineralization of hypersaline produced water using microbially induced calcite precipitation. *Water Res.* 190. <https://doi.org/10.1016/j.watres.2020.116753>.
- Kang, W., Kang, X., Lashari, Z.A., Li, Z., Zhou, B., Yang, H., Sarsenbekuly, B., Aidarova, S., 2021. Progress of polymer gels for conformance control in oilfield. *Adv. Colloid Interf. Sci.* <https://doi.org/10.1016/j.cis.2021.102363>.
- Kim, D.H., Mahabadi, N., Jang, J., van Paassen, L.A., 2020. Assessing the kinetics and pore-scale characteristics of biological calcium carbonate precipitation in porous media using a microfluidic chip experiment. *Water Resour. Res.* 56. <https://doi.org/10.1029/2019WR025420>.
- Kirkland, C.M., Hiebert, R., Hyatt, R., McCloskey, J., Kirksey, J., Thane, A., Cunningham, A.B., Gerlach, R., Spangler, L., Phillips, A.J., 2021. Direct injection of biomineralizing agents to restore injectivity and wellbore integrity. *SPE Production and Operations* 36, 216–223. <https://doi.org/10.2118/203845-PA>.
- Konstantinou, C., Wang, Y., 2023. Unlocking the potential of microbially induced calcium carbonate precipitation (MICP) for hydrological applications: a review of opportunities, challenges, and environmental considerations. *Hydrology* 10, 178. <https://doi.org/10.3390/hydrology10090178>.
- Kralj, D., Breevi, L., Kontrec, J., 1997. Vaterite growth and dissolution in aqueous solution III. Kinetics of transformation. *J. Cryst. Growth.* 177 (3–4), 248–257.
- Li, Y., Sarlyer, O.S., Ramachandran, A., Panyukov, S., Rubinstein, M., Kumacheva, E., 2015. Universal behavior of hydrogels confined to narrow capillaries. *Sci. Rep.* 5. <https://doi.org/10.1038/srep17017>.
- Lioliou, M.G., Paraskeva, C.A., Koutsoukos, P.G., Payatakes, A.C., 2007. Heterogeneous nucleation and growth of calcium carbonate on calcite and quartz. *J. Colloid Interface Sci.* 308, 421–428. <https://doi.org/10.1016/j.jcis.2006.12.045>.
- Liu, N., Haugen, M., Benali, B., Landa-Marbán, D., Fernø, M.A., 2023a. Pore-scale kinetics of calcium dissolution and secondary precipitation during geological carbon storage. *Chem. Geol.* 641. <https://doi.org/10.1016/j.chemgeo.2023.121782>.
- Liu, N., Haugen, M., Benali, B., Landa-Marbán, D., Fernø, M.A., 2023b. Pore-scale spatiotemporal dynamics of microbial-induced calcium carbonate growth and distribution in porous media. *International Journal of Greenhouse Gas Control* 125. <https://doi.org/10.1016/j.ijggc.2023.103885>.
- Ma, L., Pang, A.P., Luo, Y., Lu, X., Lin, F., 2020. Beneficial factors for biomineralization by ureolytic bacterium *Sporosarcina pasteurii*. *Microb. Cell Factories* 19. <https://doi.org/10.1186/s12934-020-1281-z>.
- Minto, J.M., Hingerl, F.F., Benson, S.M., Lunn, R.J., 2017. X-ray CT and multiphase flow characterization of a ‘bio-grouted’ sandstone core: the effect of dissolution on seal longevity. *International Journal of Greenhouse Gas Control* 64, 152–162. <https://doi.org/10.1016/j.ijggc.2017.07.007>.
- Mortensen, B.M., Haber, M.J., DeJong, J.T., Caslake, L.F., Nelson, D.C., 2011. Effects of environmental factors on microbial induced calcium carbonate precipitation. *J. Appl. Microbiol.* 111, 338–349. <https://doi.org/10.1111/j.1365-2672.2011.05065.x>.
- Nanne, E.E., Aucoin, C.P., Leonard, E.F., 2010. Shear rate and hematocrit effects on the apparent diffusivity of urea in suspensions of bovine erythrocytes. *ASAIO J.* 56, 151–156. <https://doi.org/10.1097/MAT.0b013e3181d4ed0f>.
- Nasvi, M.C.M., Ranjith, P.G., Sanjayan, J., 2013. The permeability of geopolymer at down-hole stress conditions: application for carbon dioxide sequestration wells. *Appl. Energy* 102, 1391–1398. <https://doi.org/10.1016/j.apenergy.2012.09.004>.
- Phillips, A.J., Gerlach, R., Lauchnor, E., Mitchell, A.C., Cunningham, A.B., Spangler, L., 2013. Engineered applications of ureolytic biomineralization: a review. *Biofouling*. <https://doi.org/10.1080/08927014.2013.796550>.
- Phillips, A.J., Troyer, E., Hiebert, R., Kirkland, C., Gerlach, R., Cunningham, A.B., Spangler, L., Kirksey, J., Rowe, W., Esposito, R., 2018. Enhancing wellbore cement integrity with microbially induced calcite precipitation (MICP): a field scale demonstration. *J. Pet. Sci. Eng.* 171, 1141–1148. <https://doi.org/10.1016/j.petrol.2018.08.012>.
- Pokrovsky, O.S., 1998. Precipitation of calcium and magnesium carbonates from homogeneous supersaturated solutions. *J. Cryst. Growth.* 186 (1–2), 233–239.
- Pokrovsky, O.S., Golubev, S.V., Schott, J., 2005. Dissolution kinetics of calcite, dolomite and magnesite at 25 °C and 0 to 50 atm pCO₂. *Chem. Geol.* 217, 239–255. <https://doi.org/10.1016/j.chemgeo.2004.12.012>.
- Song, C., Elsworth, D., Jia, Y., Lin, J., 2022. Permeable rock matrix sealed with microbially-induced calcium carbonate precipitation: evolutions of mechanical behaviors and associated microstructure. *Eng. Geol.* 304, 106697. <https://doi.org/10.1016/j.enggeo.2022.106697>.

- Song, W., Kovscek, A.R., 2015. Functionalization of micromodels with kaolinite for investigation of low salinity oil-recovery processes. *Lab Chip* 15, 3314–3325. <https://doi.org/10.1039/c5lc00544b>.
- Song, W., Kovscek, A.R., 2016. Direct visualization of pore-scale fines migration and formation damage during low-salinity waterflooding. *J. Nat. Gas Sci. Eng.* 34, 1276–1283.
- Song, W., Kovscek, A.R., 2019. Spontaneous clay pickering emulsification. *Colloids Surf. A Physicochem. Eng. Asp.* 577, 158–166.
- Song, W., De Haas, T.W., Fadaei, H., Sinton, D., 2014. Chip-off-the-old-rock: the study of reservoir-relevant geological processes with real-rock micromodels. *Lab Chip* 14, 4382–4390. <https://doi.org/10.1039/c4lc00608a>.
- Song, W., Ogunbanwo, F., Steinsbo, M., Ferno, M., Kovscek, A.R., 2018. Mechanisms of multiphase reactive flow using biogenically calcite-functionalized micromodels. *Lab Chip* 18, 3881–3891.
- Xia, S., Davletshin, A., Song, W., 2023. Enhanced oil recovery through microbially induced calcium carbonate precipitation. *Energy Fuel* 37, 14666–14673. <https://doi.org/10.1021/acs.energyfuels.3c02027>.
- Xiao, Y., He, X., Wu, W., Stuedlein, A.W., Evans, T.M., Chu, J., Liu, H., van Paassen, L.A., Wu, H., 2021. Kinetic biomineralization through microfluidic chip tests. *Acta Geotech.* 16, 3229–3237. <https://doi.org/10.1007/s11440-021-01205-w>.
- Yu, T., Souli, H., Pechaud, Y., Fleureau, J.-M., 2021. Review on engineering properties of MICP-treated soils. *Geomechanics and Engineering* 27, 13–30. <https://doi.org/10.12989/gae.2021.27.1.013i>.
- Zhang, J., Shi, X., Chen, X., Huo, X., Yu, Z., 2021. Microbial-induced carbonate precipitation: a review on influencing factors and applications. *Advances in Civil Engineering*. <https://doi.org/10.1155/2021/9974027>.